Direct imaging of micrometer-thick interfaces in salt–salt aqueous biphasic systems

PNAS RESEARCH ARTICLE | CHEMISTRY

Direct imaging of micrometer-thick interfaces in salt–salt aqueous biphasic systems

Damien Degoulange[a,b,c], Raj Pandya[d,e], Michael Deschamps[c,f], Dhyllan A. Skiba[g], Betar M. Gallant[g], Sylvain Gigan[d], Hilton B. de Aguiar[d], and Alexis Grimaud[a,b,c,h,1]

Edited by David Weitz, Harvard University, Cambridge, MA; received December 5, 2022; accepted March 26, 2023

Unlike the interface between two immiscible electrolyte solutions (ITIES) formed between water and polar solvents, molecular understanding of the liquid–liquid interface formed for aqueous biphasic systems (ABSs) is relatively limited and mostly relies on surface tension measurements and thermodynamic models. Here, high-resolution Raman imaging is used to provide spatial and chemical resolution of the interface of lithium chloride - lithium bis(trifluoromethanesulfonyl)imide - water (LiCl–LiTFSI–water) and HCl–LiTFSI–water, prototypical salt–salt ABSs found in a range of electrochemical applications. The concentration profiles of both TFSI anions and water are found to be sigmoidal thus not showing any signs of a positive adsorption for both salts and solvent. More striking, however, is the length at which the concentration profiles extend, ranging from 11 to 2 µm with increasing concentrations, compared to a few nanometers for ITIES. We thus reveal that unlike ITIES, salt–salt ABSs do not have a molecularly sharp interface but rather form an interphase with a gradual change of environment from one phase to the other. This knowledge represents a major stepping-stone in the understanding of aqueous interfaces, key for mastering ion or electron transfer dynamics in a wide range of biological and technological settings including novel battery technologies such as membraneless redox flow and dual-ion batteries.

aqueous biphasic system | liquid–liquid phase separation | liquid–liquid interface | Gibbs adsorption | Raman imaging

Significance

Phase separation between oil and water is a well-known process. However, recent findings have shown that phase separation can also take place between two aqueous phases composed of two different dissolved salts. Such aqueous biphasic systems (ABSs) have applications both in life sciences and industrial processes. Yet, very little is known about the composition and the structure of their interfaces. Here, through direct Raman imaging, we provide visualization of ABSs interfaces and show that they are made of a concentration gradient along several microns. This large interphase contrasts with the nanometer size, molecularly sharp interface formed between water and oil. Our results lay the foundation for understanding water–water interfaces and mastering interfacial reactions relying on ion and/or electron transfer.

Liquid–liquid phase separation (LLPS) lies at the heart of chemistry both in the natural world, e.g., the membraneless separation of dense and dilute phases of macromolecules inside cells (1, 2), and in industrial systems, e.g., for chemical extraction and purification steps (3). One ubiquitous example of LLPS is that of aqueous biphasic systems (ABSs), also called aqueous two-phase systems (ATPSs), with a plethora of applications ranging from biomedicine to metal recycling (4–10). Typically, ABSs consist of two coexisting immiscible phases composed of only one solvent (water) with the phase separation driven by solutes. Many solutes have been found to drive such phase separation including polymers (5, 10), proteins (11), and ionic liquids (IL) (12). For most solutes, the phase separation was explained by the hydrophobicity of the large molecules (polymers) or the ability of ions to disturb or structure the hydrogen bonding network in water, i.e., chaotropic and kosmotropic effects, respectively (8, 13, 14). Recently, lithium halide - lithium bis(trifluoromethanesulfonyl)imide - water (LiX-LiTFSI-water with X = Cl^-, Br^-, or I^-) salt–salt ABSs, using common alkali cations but anions with large size asymmetry (thus the need to pair TFSI anions with smaller halide anions, both in large concentration, to form the biphasic system) were reported (15, 16). Such salt–salt ABSs are regarded as promising alternatives to "classical" liquid electrolytes used in battery technologies. Indeed, they can tackle problematic chemical crosstalk mechanisms observed in Li-ion/sulfur batteries (17) or even enable the assembly of promising novel battery systems such as membraneless redox flow batteries (18–20) or dual-ion batteries (21).

However, for salt–salt ABSs to be efficiently implemented in electrochemical devices, mastering the ion transfer at liquid–liquid interface is critical as it directly controls the (dis) charging rate by inducing an interfacial overpotential if too slow or can induce self-discharge when not selective. Despite this key role, interfaces of ABSs are poorly understood, almost entirely via surface tension measurements (22–25). Classically, the surface tension between two phases α and β is captured by the Gibbs adsorption equation:

$$d\gamma = -\sum_J \Gamma_J d\mu_J, \quad [1]$$

with γ being the surface tension between the two phases, Γ_J the surface excess concentration compared to the Gibbs dividing surface, and μ_J the chemical potential of the different

The Manuscript was deposited as a Preprint on ChemRxiv (CC BY-NC-ND 4.0): https://doi.org/10.26434/chemrxiv-2022-gd84k.

Author contributions: D.D. and A.G. designed research; D.D., R.P., M.D., and D.A.S. performed research; D.D., R.P., M.D., D.A.S., B.M.G., S.G., and H.B.d.A. analyzed data; D.D., R.P., M.D., D.A.S., B.M.G., S.G., H.B.d.A., and A.G. edited the manuscript and discussed the results; and D.D., R.P., and A.G. wrote the paper.

The authors declare no competing interest.

This article is a PNAS Direct Submission.

[1]To whom correspondence may be addressed. Email: alexis.grimaud@bc.edu.

This article contains supporting information online at https://www.pnas.org/lookup/suppl/doi:10.1073/pnas.2220662120/-/DCSupplemental.

Published April 17, 2023.

species J in solution (26). Noting that $\mu_J = \mu_J^0 + RT\ \ln(a_J)$, the surface excess concentration can be expressed as:

$$\Gamma_S = -\frac{a_S}{RT}\left(\frac{\partial\gamma}{\partial a_S}\right)_{T,J\neq S}, \quad [2]$$

linking the surface tension to the adsorption of species at the interface (26). If by increasing the activity of species *S* the surface tension decreases (i.e., $\left(\frac{\partial\gamma}{\partial a_S}\right) < 0$), then $\Gamma_S > 0$ and the species *S* is accumulated at the interface (positive adsorption—Fig. 1*A*). However, if by increasing the activity of species *S* the surface tension increases (i.e., $\left(\frac{\partial\gamma}{\partial a_S}\right) > 0$), then $\Gamma_S < 0$ and the species S is depleted at the interface (negative adsorption—Fig. 1*B*) (26). The thickness of the interface can be defined as the length across which the negative (or positive) adsorption takes place.

In contrast to ABSs, interfaces between two immiscible electrolyte solutions (ITIES), such as between water and nitrobenzene or other polar solvents, have been widely studied. They are known to be molecularly sharp with a positive adsorption of ions over only a few nanometers at the interface (Fig. 1*C*), as demonstrated by a combination of surface tension, capacitance, and surface-sensitive spectroscopic methods (27–30). This picture of the ITIES was essential toward developing new applications based on ion (31, 32) or electron transfer (33, 34) such as coupling reactions (35) or electrosynthesis (36) at the interface. Thus, for ABSs to reach their full potential, a deeper understanding of their interfaces is critical (Fig. 1*D*). Yet, the requirement of nanoscale chemical sensitivity means, to the best of our knowledge, that no experimental visualization of any aqueous-aqueous interfaces has yet been reported, with information regarding their composition remaining generally sparse. In this work, we use a unique combination of variable temperature nuclear magnetic resonance (VT-NMR) and high-spatial-resolution Raman imaging to resolve and understand the interface of salt–salt ABSs. Studying the LiCl–LiTFSI–water and the HCl–LiTFSI–water systems, we provide the demonstration for a negative adsorption of ions and water at the interface. Strikingly, we reveal a continuous, microscale change of chemical environment, fundamentally different from the nanoscale, molecularly sharp ITIES. Our results call for the reinvestigation of previously known ABSs using chemically sensitive imaging/spectroscopic methods and to, more broadly, study the structure and dynamics of liquid–liquid interfaces.

Results

Phase Diagram, Surface Tension, and Temperature Behavior of the LiCl–LiTFSI–Water System. To first understand the composition demixing for the LiCl–LiTFSI–water system, the phase diagram was obtained via the cloud point titration technique (*Materials and Methods*). As shown in Fig. 2*A*, the phase diagram shows a binodal curve separating the monophasic region (purple) from the biphasic one (red) (15, 16). The interfacial tension for the LiCl–LiTFSI–water systems was measured from the drop-weight method (*Materials and Methods*) using Tate's law with Harkins and Brown correction (37) (Fig. 2*B*). For the 5 m (mol. kg^{-1}) LiTFSI–10 m LiCl biphasic system, the interfacial tension is estimated as ≈ 3 $mN.m^{-1}$. This value is similar to IL–salt ABSs (0.4 to 2.3 $mN.m^{-1}$) (25) but 10 times lower than values reported for ITIES (20 to 30 $mN.m^{-1}$) (27) and higher than that reported for polymer–polymer ABSs (0.01 to 500 $\mu N.m^{-1}$) (22, 38). Decreasing the molalities to 3 m LiTFSI–6 m LiCl, the interfacial tension decreases down to values 200 $\mu N.m^{-1}$. When plotting the interfacial tension as a function of the difference between salts total molality from these systems and the binodal curve at 2.6 m LiTFSI–5.2 m LiCl (Δm, Fig. 2*B*), the surface tension tends to zero when reaching the binodal curve, i.e., for Δm = 0. This result agrees with the system becoming monophasic on crossing the binodal curve, hence having no interfacial tension. According to Eq. **2**, this increasing interfacial tension with increasing molality suggests either that salts have a negative adsorption at the interface, as schematized in Fig. 1*B*, or that water has a positive adsorption, as schematized in Fig. 1*A*, or both.

The top and bottom phases collected from the 5 m LiTFSI–10 m LiCl biphasic system were characterized by infrared spectroscopy (Fig. 2 *C* and *D*). By looking at the TFSI peaks at 1,340, 1,190, 1,125, and 1,050 cm^{-1} (Fig. 2*C*), the top phase is found to be nearly depleted in TFSI anions while the bottom phase is rich in TFSI (15). In Fig. 2*D*, the peak at 3,365 cm^{-1} and the shoulder at 3,230 cm^{-1} corresponding to OH vibrations for water molecules with strong hydrogen bonding network ($OH_{strong\text{-}HB}$) are only observed for the top phase (39, 40). In contrast, the bottom phase shows a band at 3,570 cm^{-1} previously ascribed to OH vibrations for water with weaker hydrogen bonding network resembling that of the so-called water-in-salt systems, i.e., a TFSI-rich environment ($OH_{weak\text{-}HB}$) (40, 41). The bottom phase is thus richer in TFSI when compared to the top one, indicating a high ion partition coefficient. By decreasing the concentration close to the binodal curve and studying the 2.6 m LiTFSI–5.2 m LiCl system (Fig. 2 *E* and *F*), vibrations associated with the top and the bottom phases are found qualitatively similar, however with the intensities of the TFSI peaks still being modestly higher in the bottom phase, thus resulting in a low ion partition coefficient (Fig. 2*E*). Moreover, Fig. 2*F* shows that the intensity of the shoulder in the region of the $OH_{weak\text{-}HB}$ vibrations is constant for both phases. Only a slight decrease in the region corresponding to $OH_{strong\text{-}HB}$ vibrations intensity, linked to a weakening of the water–water hydrogen bonding network, is

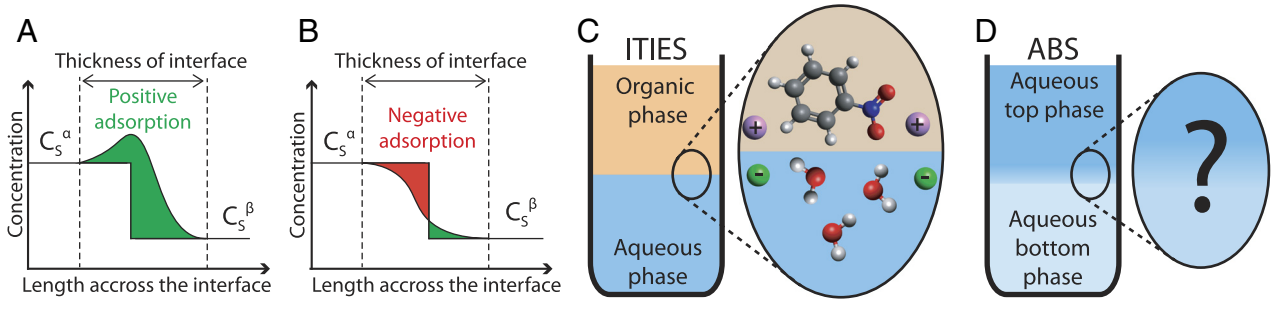

Fig. 1. Description of the different types of liquid–liquid interfaces. (*A* and *B*) Schematic depicting the concentration profile of a solute (S) from phase α (C_s^{α}) to phase β (C_s^{β}) across an interface for positive (*A*) and negative (*B*) adsorption. Green and red represent, respectively, positive and negative integrals when compared to a step change of concentration. (*C* and *D*) Cartoons of ITIES (*C*) and ABSs (*D*) interfaces.

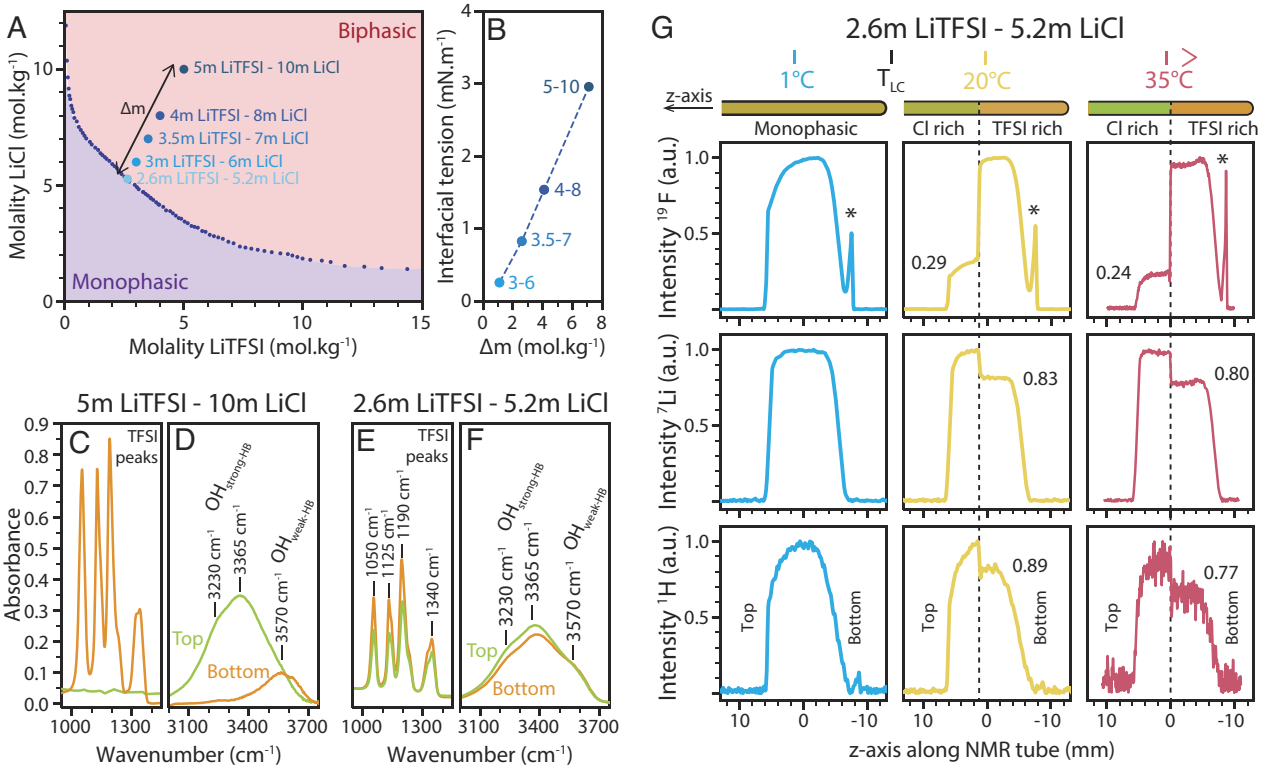

Fig. 2. LiCl–LiTFSI–water system description. (*A*) Phase diagram of the LiCl–LiTFSI–water system with the monophasic region in purple and the biphasic region in red. X m LiTFSI–Y m LiCl systems are studied along the line 2X = Y, as indicated with blue dots. Along this line, the binodal curve is crossed at 2.6 m LiTFSI–5.2 m LiCl. (*B*) Interfacial tensions for the LiCl–LiTFSI–water system as function of the salts total molality differential to the binodal curve in moles per kg (Δm), i.e., Δm=(X+Y)−(2.6+5.2). (*C* and *D*) Infrared spectra recorded for the 5 m LiTFSI–10 m LiCl system for TFSI vibrations (*C*) and OH vibrations (*D*) with top phase in green and the bottom phase in orange. (*E* and *F*) Infrared spectra for the 2.6 m LiTFSI–5.2 m LiCl system for TFSI vibrations (*E*) and OH vibrations (*F*) with the top phase in green and the bottom phase in orange. (*G*) VT-NMR analysis of the 2.6 m LiTFSI–5.2 m LiCl systems at 1 °C (blue), 20 °C (yellow), and 35 °C (red) for the nucleus ^{19}F (*Top*), ^{7}Li (*Middle*) , and ^{1}H (*Bottom*) along the height of the NMR tube from left (top of the tube) to right (bottom of the tube). The peak highlighted by * is associated with polytetrafluoroethylene component of the NMR probehead (See *Materials and Methods*).

found in the bottom phase. Overall, infrared spectroscopy indicates that when moving away from the binodal curve, i.e., as the interfacial tension increases, there is greater ion partition between the two immiscible phases.

To probe the influence of temperature on salt–salt ABSs interface, the 2.6 m LiTFSI–5.2 m LiCl system was studied between 0 °C and 35 °C. Upon cooling from room temperature to a temperature close to 0 °C, the system reversibly switches from biphasic to monophasic, forming a so-called lower critical temperature (T_{LC}) system, as confirmed by reaction microcalorimetry (*SI Appendix*, Fig. S1 and *Supplementary Discussion* 1) (26, 42). VT-NMR was used to provide spatially resolved information across the ABS interface (z-axis, *SI Appendix*, Fig. S2) and to assess the ion partition as function of temperature (Fig. 2*G*). At 35 °C, the intensity profile for ^{19}F shows a sharp difference across the interface, with more TFSI found in the bottom phase than in the top phase (Fig. 2 *G*—*Right* panels in red), in agreement with the infrared spectroscopy data (Fig. 1 *E* and *F*). Similarly, the intensity profiles for ^{7}Li and ^{1}H show the top phase, i.e., the TFSI-poor one, to be richer in lithium and protons. By lowering the temperature to 20 °C, the partitions for Li^+ and TFSI ions and for water decrease (Fig. 2 *G*—*Middle* panels in yellow). Finally, at 1 °C, the system is monophasic and the solution is found to be homogeneous (Fig. 2 *G*—*Left* panels in blue). Therefore, the ion partition decreases when decreasing the temperature, eventually crossing the binodal curve and forming a monophasic system at low temperature. For systems far from the binodal curve, i.e., 5 m LiTFSI–10 m LiCl, much larger ion and water partitions are recorded at room temperature, as seen in Fig. 2 *C* and *D*, and no transition from biphasic to monophasic was observed between −15 °C and 80 °C.

Physical Properties of the Interface in the LiCl–LiTFSI–Water System. In order to gain a microscopic understanding of the interface composition, Raman imaging was performed (lateral resolution ≈300 nm; axial resolution ≈800 nm, spectral resolution ≈15 cm^{-1}), taking advantage of the different phase-dependent vibrations for TFSI anions and water. Fig. 3*A* shows false-color images of the integrated intensity of the TFSI peak at ≈740 cm^{-1} for the 2.6 m LiTFSI–5.2 m LiCl system, with increasing TFSI concentration shown from blue to red. Comparing the Raman spectra collected across the interface (Fig. 3*B*) reveals a continuous change of the spectra, indicating a gradient of chemical compositions and solvation environments (behavior also seen in Fig. 3*C* for OH vibrations).

The Raman spectra were deconvoluted into their respective components to obtain qualitative chemical insight into the changes occurring across the interface. Based on previous studies (41, 43, 44), the TFSI band can be decomposed into three components (Fig. 3 *D* and *E* and *SI Appendix*, Figs. S3 and S4). The TFSI-rich phase is mostly composed of components corresponding to mono- (contact ion pairs (CIP), 738 cm^{-1}) and bi-coordinated (aggregates (Agg), 743 cm^{-1}) TFSI ions with a limited contribution from "free" TFSI ions (725 cm^{-1}). Moving from the TFSI-rich phase (Fig. 3*D*) to the TFSI-poor phase (Fig. 3*E*), the intensity of the bi-coordinated component gradually drops alongside that of the

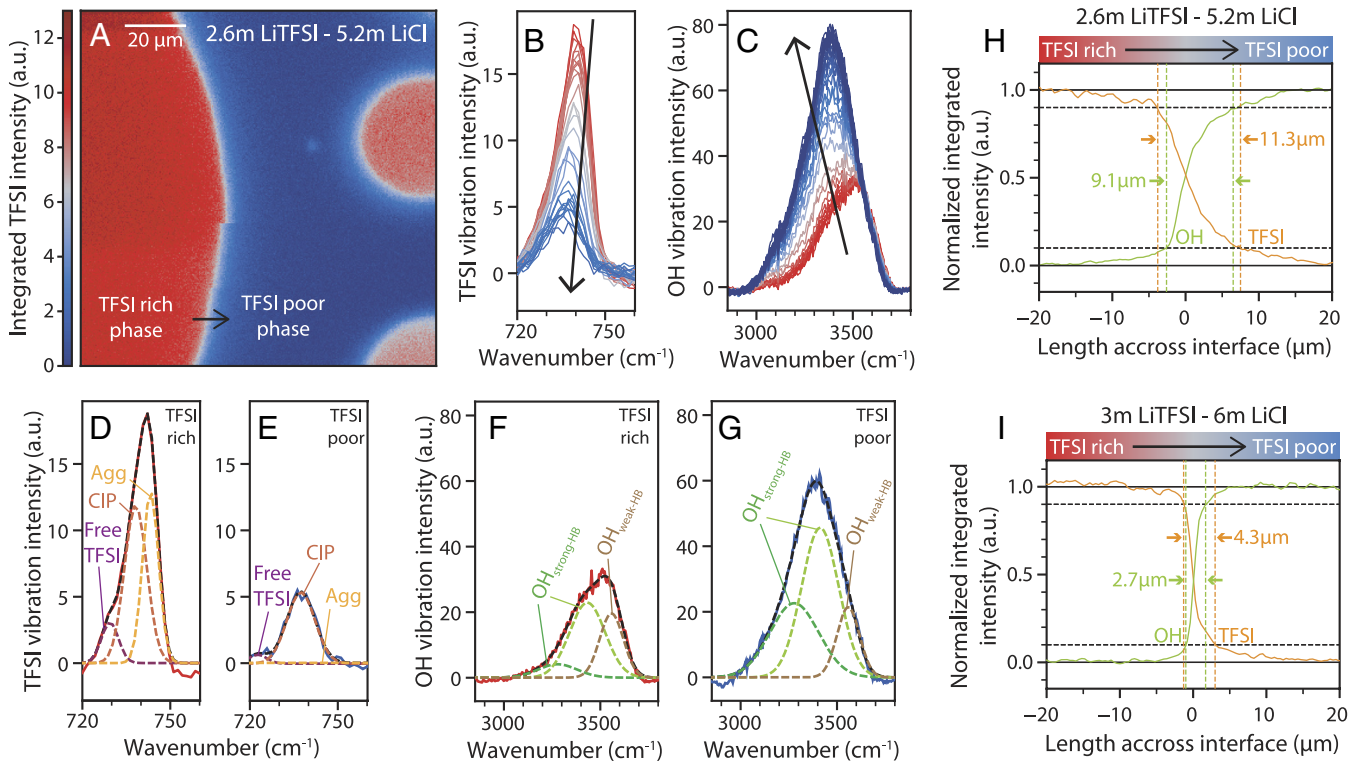

Fig. 3. Raman imaging across the interface of the 2.6 m LiTFSI–5.2 m LiCl and 3 m LiTFSI–6 m LiCl systems. (*A*) Raman imaging of the 2.6 m LiTFSI–5.2 m LiCl system generated by integration of the TFSI vibrations. A slight movement of the liquid during imaging results in a partial shift in the image (≈50 μm from bottom); the top and bottom parts of the image are hence not compared. (*B* and *C*) Raman spectra collected across the interface for TFSI vibrations (*B*) and for OH vibrations (*C*) of the 2.6 m LiTFSI–5.2 m LiCl system. The color of plots matches that in (*A*). (*D* and *E*) Peak decomposition of the TFSI vibrations in the TFSI-rich phase (*D*) and TFSI-poor phase (*E*) of the 2.6 m LiTFSI–5.2 m LiCl system. (*F* and *G*) Peak decomposition of the OH vibrations in the TFSI-rich phase (*F*) and TFSI-poor phase (*G*) of the 2.6 m LiTFSI–5.2 m LiCl system. (*H*) The normalized intensity of OH (green) and TFSI (orange) vibrations across the interface of the 2.6 m LiTFSI–5.2 m LiCl system. (*I*) The normalized intensity of OH (green) and TFSI (orange) vibrations across the interface of the 3 m LiTFSI–6 m LiCl system.

free TFSI component, while the intensity of the mono-coordinated TFSI component is still present but at a lower intensity (*SI Appendix*, Fig. S4). Similarly, the OH band can be decomposed into several components (39–41, 45–47) (Fig. 3 *F* and *G* and *SI Appendix*, Figs. S3–S5). Using the simplest model that fits our data, the water spectra were fitted with three components. Two components at 3,270 cm^{-1} and at 3,430 cm^{-1} correspond to the $OH_{strong\text{-}HB}$ interactions from the water hydrogen bonding network, described in the literature as ice-like and ice-like liquid components (45, 46) or as double and single H-bounded water molecules (47). The last component at 3,560 cm^{-1} is referred to in the literature as a liquid-like amorphous phase components (45, 46) or water molecules without H-bound (47), thus corresponding to $OH_{weak\text{-}HB}$ interactions from a TFSI-rich environment. When crossing from the TFSI-rich (Fig. 3*F*) to the TFSI-poor phase (Fig. 3*G*), the intensity of the components associated with a strong hydrogen bonding between water molecules increases ($OH_{strong\text{-}HB}$, low wavenumber components), while the intensity of the component associated with weaker water interactions remains approximately constant ($OH_{weak\text{-}HB}$, high wavenumber component) (*SI Appendix*, Fig. S4). Together, the Raman peak deconvolutions reveal that the interface is composed of a continuum of solvation environments gradually switching from a solvation structure previously ascribed to water-in-salt electrolytes (TFSI-rich phase with weak hydrogen bonding between water molecules and with TFSI aggregates) to that of a more classical salt-in-water electrolyte (TFSI-poor phase with a stronger hydrogen bonding network between water molecules and without TFSI aggregates). We note that as the polarization of our pump and detected Raman light is poorly defined (owing to imaging with high numerical apertures) we refrain from more quantitative analysis.

By plotting the normalized integrated Raman intensity variation and peak decomposition parameters across the interface for TFSI and OH vibrations, a sigmoidal curve is obtained (Fig. 3*H* and *SI Appendix*, Fig. S4). This observation suggests that both the solvent, i.e., water, and one of the solutes, i.e., TFSI anions, have a negative adsorption at salt–salt ABSs interface (Eq. **2** and Fig. 1*B*). More importantly, the thickness of the ABS interface is deduced by measuring the length over which the negative adsorption takes place, which is estimated by the distance necessary to increase from 10 to 90% of the normalized integrated Raman intensity. For the 2.6 m LiTFSI–5.2 m LiCl system, the thickness is estimated to be 9.1 μm and 11.3 μm from the OH and the TFSI vibrations, respectively. The estimated thickness was found to be stable over hours and between multiple samples, reflecting a steady state (*SI Appendix*, Fig. S6). Such a large thickness cannot be explained by the existence of thermal capillary waves whose height we estimate to be of only several nanometers (48) (*SI Appendix*, Fig. S7). Nor can such a large thickness be a result of droplet curvature, refractive index mismatches (49), or limitations in our lateral resolution of such large curved interfaces (≈800 nm). Indeed, we are able to measure molecularly sharp ITIES such as water–hexanone (50) or water–dichloroethane (27–30) down to a size of ≈1 μm (*SI Appendix*, Fig. S8). Furthermore, the curvature of the interfaces is far larger (10 times) than the axial resolution of our laser system (≈800 nm) as shown in *SI Appendix*, Fig. S9 where a three-dimensional reconstruction of the different phase regions is built (51). Consequently, the interfaces can be approximated as a vertical slab with thickness effects ignored.

Having postulated the negative adsorption of TFSI anions and water molecules at the interface of a system close to the binodal

curve, similar studies were carried out for systems with greater concentrations. For a 3 m LiTFSI–6 m LiCl system (Fig. 3*I* and *SI Appendix*, Fig. S10), a gradual change in solvation environment is observed when crossing the interface, similar to that of the 2.6 m LiTFSI–5.2 m LiCl system. The sigmoidal curve observed for the integrated intensity (Fig. 3*I*) again suggests the negative adsorption of both TFSI and water even at higher molalities. The thickness of the interface was estimated to be 2.7 µm and 4.3 µm from the OH and the TFSI vibrations, respectively, smaller than previously measured for the 2.6 m LiTFSI–5.2 m LiCl system (Fig. 3*H*). Systems with greater concentrations are reported in *SI Appendix*, Fig. S10, showing an interface of about 3 µm and 2.5 µm for the 4 m LiTFSI–8 m LiCl and 5 m LiTFSI–10 m LiCl systems, respectively. Overall, we establish that for a system with a T_{LC}, by increasing salt molalities, i.e., moving away from the binodal curve, the interface gets thinner from about 10 µm down to the resolution of our measurement of a few microns.

Interface for Upper Critical Solution Temperature: The HCl–LiTFSI–Water System. The above results were then compared with those for HCl–LiTFSI systems (*SI Appendix*, Fig. S11) where VT-NMR (*SI Appendix*, Fig. S12) and reaction microcalorimetry (*SI Appendix*, Fig. S13) measurements reveal an upper critical temperature (T_{UC}) (26, 42), i.e., the system becomes miscible upon heating. As for the LiCl–LiTFSI–water systems, Raman imaging carried out on flat interfaces reveals that the solvation environment changes gradually over a few microns from one phase to the other (Fig. 4). Going from the TFSI-rich to the TFSI-poor phase, the spectral components at lower frequency, corresponding to strong hydrogen bonding, are found to increase for OH vibrations (Fig. 4*C* and *SI Appendix*, Fig. S14) along with an increase of the high-frequency components corresponding to mono- and bi-coordinated TFSI anions (Fig. 4*B* and *SI Appendix*, Fig. S14). The concentration-position profile for TFSI anions and water across the interface are both found to be sigmoidal in shape (Fig. 4*D*). Hence, independent of whether a given system has a T_{LC} or a T_{UC}, a negative adsorption is suggested for the solute and the solvent. Repeating measurements at different concentrations, it is found that the interfacial thickness decreases with increasing molality (≈ 5 µm for 5 m LiTFSI–10 m HCl system, Fig. 4*D* and ≈ 2 µm for 6 m LiTFSI–12 m HCl system, *SI Appendix*, Fig. S15), as for the LiCl–LiTFSI–water system.

Our results show that, unlike ITIES, salt–salt ABSs interfaces cannot be considered as molecularly sharp interfaces. Rather, they are microns-thick interphases forming a continuous gradient between both liquid phases. Given that the interfacial tension of salt–salt ABSs (about few $mN.m^{-1}$) lies between that of ITIES (tens of $mN.m^{-1}$) and polymer–polymer ABSs interfaces (hundreds of $\mu N.m^{-1}$) which both have interfaces on the sub-800 nm scale, our results show that salt–salt ABSs are outliers. Based on our findings, models that have been developed for ITIES using molecular isotherms, which link molecular interactions, surface tension, and interfacial thickness, hence do not appear appropriate for describing ABS. One way to qualitatively reconcile our observations is via the Gibbs adsorption equation (Eq. **1**) which does not take interfacial thickness or molecular interactions into account. Thus, when transitioning from a dilute regime to a concentrated regime, as it is the case for both the LiTFSI and LiCl solutions studied in this work, the activity of water decreases unlike the activities of ions that are increasing, as previously shown for Li^+ activity in both LiTFSI and LiCl solutions (52) and for LiTFSI/LiBETI solutions (53), as well as plotted for LiCl (54–56) in *SI Appendix*, Fig. S16. Furthermore, the increase of the salt activity with concentration is much greater than the decrease of the activity of water. Hence, according to the Gibbs adsorption equation (Eq. **1**), and bearing in mind that our results suggest a negative adsorption of species at the interface ($\Gamma_S < 0$) and that the surface tension increases with the salt concentration, one can thus conclude that the change in surface tension is dominated by the increase of the activity of ions rather than by the decrease of the activity of water.

However, such conclusion should be used with care as information below the micrometer scale cannot be accessed with our Raman imaging (*SI Appendix*, Fig. S10). More precisely, a very thin adsorption layer can still exist at the nanometer scale within the sigmoid observed by Raman imaging. In fact, such discrepancy was previously observed for the double layer formed between a conductive electrode and IL. (57, 58) Further studies are thus necessary to understand the exact nature of the electrochemical double layer at the liquid/liquid interface formed in ABS.

Summarizing the different systems studied in this work, we find that the thickness of the interface is decreasing with both total molality (Fig. 5*A* and *SI Appendix*, Fig. S17) and surface tension (Fig. 5*B*). For large molality, i.e., for high surface tension (Fig. 5*C*), we observe large ion partitioning while Raman imaging reveals thin interfaces. Decreasing the molality, i.e., for lower surface tension, the ion partitioning is smaller but the thickness of the interface increases (Fig. 5*D*). However, a more quantitative interpretation of the Gibbs adsorption equation, relating surface excess to surface tension, requires a simultaneous knowledge of the concentration profiles for all species, currently out of reach for ions such as Cl^- or Li^+ using Raman imaging.

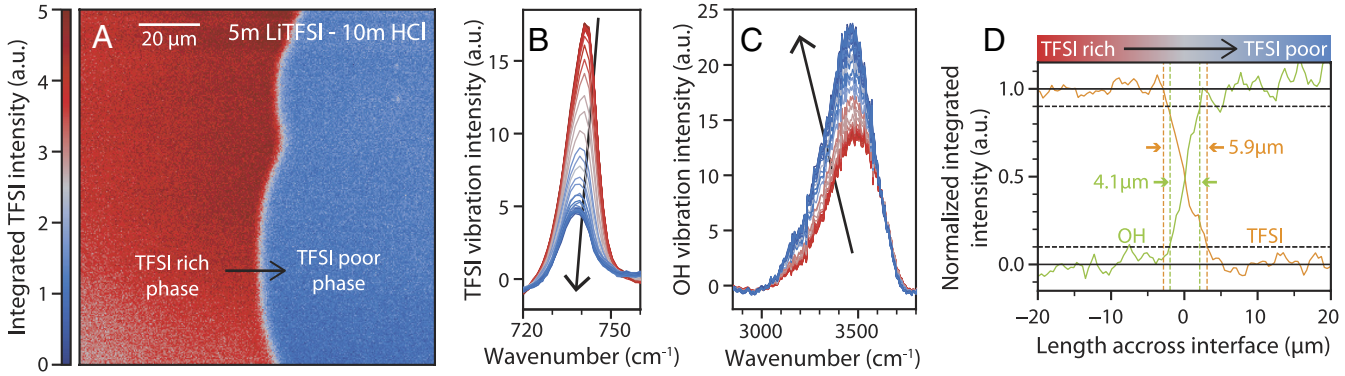

Fig. 4. Raman imaging across the interface of the 5 m LiTFSI–10 m HCl system. (*A*) Raman imaging of the 5 m LiTFSI–10 m HCl system generated by integration of the TFSI vibrations. (*B* and *C*) Raman spectra collected across the interface for the TFSI vibrations (*B*) and for OH vibrations (*C*) The color of plots matches that in (*A*). (*D*) The normalized intensity of OH (green) and TFSI (orange) vibrations across the interface.

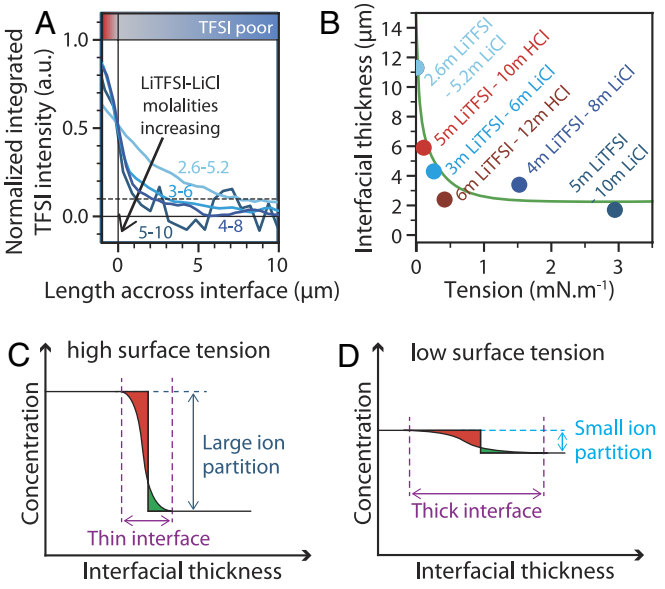

Fig. 5. Evolution of interfacial thickness as function of molality and surface tension. (*A*) Comparison of the integrated intensity for TFSI vibrations for different LiCl–LiTFSI–water systems. (*B*) Interfacial thickness as function of the interfacial tension for the LiCl–LiTFSI–water and HCl–LiTFSI–water systems studied in this work. The green line is only a guide to the eye. (*C* and *D*) Schematic depicting the concentration profile of solutes across an interface for high (*C*) and low (*D*) surface tension. Green and red represent, respectively, positive and negative integrals when compared to a step change of concentration.

Conclusion

In summary, with microscopic chemical resolution, we have directly imaged the interface formed for salt–salt ABSs as a function of concentration. Our study reveals, unlike for ITIES or polymer ABSs, very large interfacial thicknesses up to 10 μm. The thickness correlates inversely with the salts concentration and the interfacial tension. Using Raman spectroscopy, the molecular bonding environment across the interfaces was probed, demonstrating a gradual change in water structure from an environment in which the hydrogen bonding network is weak and anions aggregates exist (TFSI-rich phase) to an environment resembling more of a dilute aqueous solution (Cl-rich phase). This result highlights that both LiCl and LiTFSI are important to generate different environments resulting in the phase separation. In addition, using NMR and calorimetry methods, we dynamically probed the effect of temperature on the miscibility of salt–salt ABSs. Comparing LiCl–LiTFSI–water and HCl–LiTFSI–water systems, we find that changing the cation from Li^+ to H^+ inverts the temperature dependence, with the former becoming miscible upon cooling below room temperature while the latter becomes immiscible. Nevertheless, such opposing behavior does not dramatically change the thickness of the interface, which remains in the 1 to 10 μm range. Considering a negative adsorption for both water and solutes at the interface, we find that ion partitioning increases with salt concentration. We postulate that the formation of the interface is dictated by increased activity of solute ions with concentration. Following the insights provided by our findings, better theoretical understanding of ABSs is still needed. Indeed, the surface tension of salt–salt ABSs lies between that of ITIES and of polymer–polymer systems, yet they show much larger interfaces, beyond access for classical molecular dynamics simulations. Understanding further how the properties and size of the interfaces can be tuned is not only of fundamental interest but crucial if ABSs systems are to be used for electrochemical devices (17–21), chemical separation/purification steps (9), carbon capture (59), or in multiphase catalytic applications (60). Control over the phase diagram will allow new electrolytes with enhanced properties to be engineered, improving the efficiency of extraction, purification, and capture reactions but also opening a new avenue for designing electrochemical devices, e.g., systems that phase separate upon temperature increase such that thermal runaway processes can be shut-off (61). One important question nevertheless remaining relates to how the nature of the cations influences temperature dependence of the phase diagram for salt–salt ABSs.

Generally, probing liquid–liquid interfaces in systems—be they electrochemical, biological, or otherwise—has remained challenging. Our results demonstrate the power of Raman imaging, particularly over other popular optical imaging methods such as reflection/scattering microscopy, for providing label-free microscopic chemical information especially in material science applications. Combining such techniques with super-resolution (62) or tip-enhanced (63) approaches will allow access to the sub-100 nm resolution limit and broaden the set of systems that can be examined, e.g., polymer ABSs and phase separations at electrified interfaces. Combining more advanced Raman schemes (triple grating spectrometers, heterodyne optical Kerr effect (64)) with other techniques such as neutron reflectometry (especially deep inelastic neutron scattering) (65, 66) and sum frequency generation (67, 68) will be useful to gain an improved understanding of critical low-energy interactions such as hydrogen-bonds. The combination of these characterization techniques with novel chemistries will help unravel the complex ion transport properties across the ABSs interface, leading to new discoveries in the design of complex liquid electrolytes for membraneless electrochemical devices or phase separation. Finally, comparing transport properties across liquid–liquid interfaces with that across more traditional solid–liquid interfaces (69, 70) ubiquitous in electrochemical devices will shine a new light on how (de)solvation can be modulated to fine-tune ion-transfer dynamics.

Materials and Methods

Materials. Lithium bis(trifluoromethanesulfonyl)imide (LiTFSI Extra dry, Solvionic, 99.9%), lithium chloride (LiCl anhydrous, Alfa Aesar, 99%), and hydrochloric acid (HCl 30%, Sigma-Aldrich Suprapur) were weighed and MilliQ water was added to reach the desired molalities. Tetrabutylammonium tetraphenylborate (TBATPB, 99% Sigma-Aldrich) was weighed to reach the desired concentration in dichloroethane (DCE, 99%, Alfa Aesar). 2-Heptanone (99%, Alfa Aesar) was used as received.

Phase Diagram Construction. Phase diagrams were measured using the cloud point titration method previously described (15, 16). Briefly, starting from a known mass of a concentrated solution of one component, an aqueous solution of the second component is weighed while being added dropwise and vortexed until the solution turns cloudy. Then, water is weighed while being added dropwise and vortexed until the solution turns clear again. These steps are repeated for each point of the diagram. The diagrams were made starting from different initial LiCl, LiTFSI, and HCl concentrations especially for the HCl–LiTFSI–water system in order to prevent imprecision due to HCl evaporation.

Interfacial Tension. Interfacial tensions were measured from the drop-weight method using Tate's law with Harkins and Brown correction (37). Briefly, using a peristaltic pump (Watson-Marlow, 120U-DM2), drops of the highest density phase are slowly let fall into the lowest density phase. The average weight of a drop is deduced and surface tension is calculated according to Harkins and Brown correction. Densities were measured using an electronic density meter (Anton Paar, DMA 35 Basic).

Infrared Spectra. The infrared spectra for the LiCl–LiTFSI–water system were taken using a Nicolet iS5 FTIR spectrometer, mounted with a diamond Attenuated

Total Reflectance accessory (iD1 ATR). The background correction was performed by measuring the ambient atmosphere and each spectra was acquired from 16 scans with a 4 cm^{-1} resolution from 4,000 to 500 cm^{-1}.

VT-NMR. Pulse-field gradient stimulated echo diffusion measurements were realized on a Bruker 200 MHz wide bore spectrometer, equipped with a Diff50 gradient system and a ^{19}F-^{7}Li 8 mm insert inside a liquid-state Bruker probe. One-dimensional profiles were recorded using the improf Bruker sequence (90°-gradient-180°-gradient-acquisition), with maximum field gradient strengths of 27, 29, and 30 G/cm respectively. The signals were acquired as full echoes (1 to 1.5 ms echo times) to avoid antiphase components and make the phasing easier. The maximum theoretical resolution was around 10 to 20 µm. Recycling delays of 7, 9, and 17 s were used, with 96, 16, and 16 transients acquired for ^{1}H, ^{19}F, and ^{7}Li respectively.

Raman Imaging. The microscope was a standard layout of an epi-detected Raman microscope. A pump laser beam (wavelength = 532 nm, Newport Millenia eV) was spectrally cleaned up by a bandpass filter (FLH05532-4, ThorLabs), and its beam width was expanded to 7.2 mm before entering a home-built inverted microscope. We used high numerical aperture (NA) oil-immersion objectives (Nikon 60×/1.4NA oil) to ensure high-resolution imaging and increase collection efficiency. Pump power before the objective was 150 mW, a power level that ensured no degradation of domains within the scanned region. The samples were scanned/descanned with a set of galvanometric mirrors (ThorLabs). The Raman inelastic backscattered light was collected by the same objective and focused with the microscope tube lens on the entrance slit of the detector which acted as the effective pinhole for confocal detection. A notch filter blocked residual pump light (NF533-17, ThorLabs) before guiding the signal to the spectrometer (Andor, Shamrock 303i, grating 300 l/mm), equipped with a high-sensitivity charge-coupled camera (Andor, iXon 897). All images presented were taken with integration times/pixel in the 0.1 to 0.3 s settings range. Background subtraction of Raman spectra was performed using a modified iterative polynomial smoothing method. Peak decomposition was performed using a custom Python code and the lmfit toolbox.

Titration Microcalorimetry. The calorimetric titration measurements were completed isothermally using a power compensation microcalorimeter (Thermal Hazard Technology, µRC). Each injection was performed using an automated syringe pump tower attachment. The reference samples were 1 mL of the respective ABSs solutions, and samples were stirred to allow for uniform mixing. The partial enthalpy of mixing was found by integrating the resulting power spike upon injection of one phase into the second phase (*SI Appendix*, *Supplementary Discussion* 1).

Data, Materials, and Software Availability. The raw data of the binodal curves, surface tension measurements, infrared spectra, VT-NMR and Raman spectra are available at https://doi.org/10.5281/zenodo.7782757 (71). All other data are included in the manuscript and/or *SI Appendix*.

ACKNOWLEDGMENTS. We acknowledge the French National Research Agency for its support through the Labex STORE-EX project (ANR-10LABX-76-01) and through the projects BALWISE (ANR-19-CE05-0014). R.P. thanks Clare College, University of Cambridge for funding via a Junior Research Fellowship and Alpha A. Lee (Cambridge), Marcus Fletcher (Imperial College London), and Damien Laage (ENS) for useful discussions on the data.

Author affiliations: [a]Chimie du Solide et de l'Energie, UMR 8260, Collège de France, 75231 Cedex 05 Paris, France; [b]Sorbonne Université, 75006 Paris, France; [c]Réseau sur le Stockage Electrochimique de l'Energie, CNRS FR3459, 80039 Amiens Cedex, France; [d]Laboratoire Kastler Brossel, Ecole Normale Supérieure, Université PSL, CNRS, Sorbonne Université, Collège de France, 75005 Paris, France; [e]Department of Physics, Cavendish Laboratory, University of Cambridge, Cambridge CB3 0HE, United Kingdom; [f]CNRS, Conditions Extrêmes et Matériaux : Haute Température et Irradiation, UPR3079, Université d'Orléans, 45071 Orléans, France; [g]Department of Mechanical Engineering, Massachusetts Institute of Technology, Cambridge, MA 02139; and [h]Department of Chemistry, Merkert Chemistry Center, Boston College, Chestnut Hill, MA 02467

1. A. A. Hyman, C. A. Weber, F. Jülicher, Liquid-liquid phase separation in biology. *Annu. Rev. Cell Dev. Biol.* **30**, 39–58 (2014).
2. S. Alberti, D. Dormann, Liquid-liquid phase separation in disease. *Annu. Rev. Genetics* **53**, 171–194 (2019).
3. A. Schmidt, J. Strube, "Application and fundamentals of liquid-liquid extraction processes: Purification of biologicals, botanicals, and strategic metals" in *Kirk-Othmer Encyclopedia of Chemical Technology* (John Wiley & Sons Ltd, 2018), 1–52, 10.1002/0471238961.koe00041.
4. R. Hatti-Kaul, Aqueous two-phase systems. *Mol. Biotechnol.* **19**, 269–277 (2001).
5. A. Glyk, T. Scheper, S. Beutel, PEG–salt aqueous two-phase systems: An attractive and versatile liquid–liquid extraction technology for the downstream processing of proteins and enzymes. *Appl. Microbiol. Biotechnol.* **99**, 6599–6616 (2015).
6. J. V. D. Molino *et al.*, Different types of aqueous two-phase systems for biomolecule and bioparticle extraction and purification. *Biotechnol. Progress* **29**, 1343–1353 (2013).
7. M. Mastiani, N. Firoozi, N. Petrozzi, S. Seo, M. Kim, Polymer-salt aqueous two-phase system (ATPS) micro-droplets for cell encapsulation. *Sci. Rep.* **9**, 15561 (2019).
8. M. Iqbal *et al.*, Aqueous two-phase system (ATPS): An overview and advances in its applications. *Biol. Procedures Online* **18**, 18 (2016).
9. M. Gras *et al.*, Ionic-liquid-based acidic aqueous biphasic systems for simultaneous leaching and extraction of metallic ions. *Angew. Chem. Int. Ed.* **57**, 1563–1566 (2018).
10. A. L. Grilo, M. Raquel Aires-Barros, A. M. Azevedo, Partitioning in aqueous two-phase systems: Fundamentals, applications and trends. *Separation & Purification Rev.* **45**, 68–80 (2016).
11. B. A. Rogers *et al.*, A stepwise mechanism for aqueous two-phase system formation in concentrated antibody solutions. *Proc. Natl. Acad. Sci. U.S.A.* **116**, 15784–15791 (2019).
12. M. G. Freire *et al.*, Aqueous biphasic systems: A boost brought about by using ionic liquids. *Chem. Soc. Rev.* **41**, 4966–4995 (2012).
13. B. A. Andrews, J. A. Asenjo, Theoretical and experimental evaluation of hydrophobicity of proteins to predict their partitioning behavior in aqueous two phase systems: A review. *Separation Sci. Technol.* **45**, 2165–2170 (2010).
14. N. J. Bridges, K. E. Gutowski, R. D. Rogers, Investigation of aqueous biphasic systems formed from solutions of chaotropic salts with kosmotropic salts (salt–salt ABS). *Green Chem.* **9**, 177–183 (2007).
15. N. Dubouis *et al.*, Chasing aqueous biphasic systems from simple salts by exploring the LiTFSI/LiCl/H2O Phase Diagram. *ACS Cent. Sci.* **5**, 640–643 (2019).
16. N. Dubouis, A. France-Lanord, A. Brige, M. Salanne, A. Grimaud, Anion specific effects drive the formation of Li-salt based aqueous biphasic systems. *J. Phys. Chem. B* **125**, 5365–5372 (2021).
17. C. Yang *et al.*, Unique aqueous Li-ion/sulfur chemistry with high energy density and reversibility. *Proc. Natl. Acad. Sci. U.S.A.* **114**, 6197–6202 (2017).
18. P. Navalpotro *et al.*, Pioneering use of ionic liquid-based aqueous biphasic systems as membrane-free batteries. *Adv. Sci.* **5**, 1800576 (2018).
19. P. Navalpotro *et al.*, Critical aspects of membrane-free aqueous battery based on two immiscible neutral electrolytes. *Energy Storage Mater.* **26**, 400–407 (2020).
20. A. F. Molina-Osorio, A. Gamero-Quijano, P. Peljo, M. D. Scanlon, Membraneless energy conversion and storage using immiscible electrolyte solutions. *Curr. Opin. Electrochem.* **21**, 100–108 (2020).
21. C. Yang *et al.*, Aqueous Li-ion battery enabled by halogen conversion–intercalation chemistry in graphite. *Nature* **569**, 245–250 (2019).
22. P. Ding *et al.*, Interfacial tension in phase-separated gelatin/dextran aqueous mixtures. *J. Colloid Int. Sci.* **253**, 367–376 (2002).
23. R. H. Tromp, M. Vis, B. H. Erné, E. M. Blokhuis, Composition, concentration and charge profiles of water–water interfaces. *J. Phys. Condens. Matter* **26**, 464101 (2014).
24. M. Vis, B. H. Erné, R. H. Tromp, Chemical physics of water–water interfaces. *Biointerphases* **11**, 018904 (2016).
25. Y.-V. Phakoukaki, P. O'Shaughnessy, P. Angeli, Flow patterns of ionic liquid based aqueous biphasic systems in small channels. *Chem. Eng. Sci.* **265**, 118197 (2023).
26. P. W. Atkins, J. De Paula, Phys., *Chem* (W.H. Freeman, 2006).
27. H. H. Girault, "Charge transfer across liquid–liquid interfaces" in *Modern Aspects of Electrochemistry*, J. O. Bockris, B. E. Conway, R. E. White, Eds. (Springer, US, 1993), **vol. 25**, pp. 1–62. 10.1007/978-1-4615-2876-0_1.
28. G. C. Gschwend, A. Olaya, H. H. Girault, How to polarise an interface with ions: The discrete Helmholtz model. *Chem. Sci.* **11**, 10807–10813 (2020).
29. G. C. Gschwend, A. Olaya, P. Peljo, H. H. Girault, Structure and reactivity of the polarised liquid–liquid interface: What we know and what we do not. *Curr. Opin. Electrochem.* **19**, 137–143 (2020).
30. G. C. Gschwend, H. H. Girault, Discrete Helmholtz charge distribution at liquid-liquid interfaces: Electrocapillarity, capacitance and non-linear spectroscopy studies. *J. Electroanal. Chem.* **872**, 114240 (2020).
31. F. O. Laforge, P. Sun, M. V. Mirkin, Shuttling mechanism of ion transfer at the interface between two immiscible liquids. *J. Am. Chem. Soc.* **128**, 15019–15025 (2006).
32. N. Kikkawa, L. Wang, A. Morita, Microscopic barrier mechanism of ion transport through liquid-liquid interface. *J. Am. Chem. Soc.* **137**, 8022–8025 (2015).
33. T. Solomon, A. J. Bard, Reverse (Uphill) electron transfer at the liquid/liquid interface. *J. Phys. Chem.* **99**, 17487–17489 (1995).
34. P. Peljo, E. Smirnov, H. Girault Hubert, Heterogeneous versus homogeneous electron transfer reactions at liquid–liquid interfaces: The wrong question? *J. Electroanal. Chem.* **779**, 187–198 (2016).
35. Y.-T. Kong, S. Imabayashi, T. Kakiuchi, Two-phase azo-coupling reactions driven by phase-boundary potential across the liquid|liquid interface. *J. Am. Chem. Soc.* **122**, 8215–8219 (2000).
36. R. A. Lehane *et al.*, Electrosynthesis of biocompatible free-standing PEDOT thin films at a polarized Liquid|Liquid interface. *J. Am. Chem. Soc.* **144**, 4853–4862 (2022).
37. W. D. Harkins, F. E. Brown, The determination of surface tension (free surface energy), and the weight of falling drops: The surface tension of water and benzene by capillary height method. *J. Am. Chem. Soc.* **41**, 499–524 (1919).
38. M. Vis *et al.*, Decreased interfacial tension of demixed aqueous polymer solutions due to charge. *Phys. Rev. Lett.* **115**, 078303 (2015).
39. D. M. Carey, G. M. Korenowski, Measurement of the Raman spectrum of liquid water. *J. Chem. Phys.* **108**, 2669–2675 (1998).
40. D. Xiao *et al.*, Optimization of organic/water hybrid electrolytes for high-rate carbon-based supercapacitor. *Adv. Funct. Mater.* **29**, 1904136 (2019).

41. T. Tsurumura, Y. Hashimoto, M. Morita, Y. Umebayashi, K. Fujii, Anion coordination characteristics of ion-pair complexes in highly concentrated aqueous lithium bis(trifluoromethanesulfonyl)amide electrolytes. *Anal. Sci.* **35**, 289–294 (2019).
42. S. I. Sandler, *Models for Thermodynamic and Phase Equilibria Calculations* (Taylor & Francis, 1993).
43. W. A. Henderson *et al.*, Electrolyte solvation and ionic association: VIII. Reassessing Raman spectroscopic studies of ion coordination for LiTFSI. *J. Electrochem. Soc.* **169**, 060515 (2022).
44. T. Watkins, D. A. Buttry, Determination of Mg2+ speciation in a TFSI--based ionic liquid with and without chelating ethers using raman spectroscopy. *J. Phys. Chem. B* **119**, 7003–7014 (2015).
45. Y.-H. Zhang, C. K. Chan, Observations of water monomers in supersaturated NaClO4, LiClO4, and Mg(ClO4)2 droplets using Raman Spectroscopy. *J. Phys. Chem. A* **107**, 5956–5962 (2003).
46. J. Yin, C. Zheng, L. Qi, H. Wang, Concentrated NaClO4 aqueous solutions as promising electrolytes for electric double-layer capacitors. *J. Power Sources* **196**, 4080–4087 (2011).
47. C.-Y. Li *et al.*, Unconventional interfacial water structure of highly concentrated aqueous electrolytes at negative electrode polarizations. *Nat. Commun.* **13**, 5330 (2022).
48. D. G. A. L. Aarts, M. Schmidt, H. N. W. Lekkerkerker, Direct visual observation of thermal capillary waves. *Science* **304**, 847–850 (2004).
49. S. García-Garabal, M. Domínguez-Pérez, D. Portela, L. M. Varela, O. Cabeza, Preliminary study of new electrolytes based on [MPPyr] [TFSI] for lithium ion batteries. *J. Mol. Liquids* **363**, 119758 (2022).
50. G. Luo *et al.*, The width of the water/2-heptanone liquid–liquid interface. *Electrochem. Commun.* **7**, 627–630 (2005).
51. E. E. Diel, J. W. Lichtman, D. S. Richardson, Tutorial: Avoiding and correcting sample-induced spherical aberration artifacts in 3D fluorescence microscopy. *Nat. Protoc.* **15**, 2773–2784 (2020).
52. D. Degoulange, N. Dubouis, A. Grimaud, Toward the understanding of water-in-salt electrolytes: Individual ion activities and liquid junction potentials in highly concentrated aqueous solutions. *J. Chem. Phys.* **155**, 064701 (2021).
53. Y. Yamada *et al.*, Hydrate-melt electrolytes for high-energy-density aqueous batteries. *Nat. Energy* **1**, 1–9 (2016).
54. R. A. Robinson, The water activities of lithium chloride solutions up to high concentrations at 25°. *Trans. Faraday Soc.* **41**, 756–758 (1945).
55. W. J. Hamer, Y. Wu, Osmotic coefficients and mean activity coefficients of uni-univalent electrolytes in water at 25°C. *J. Phys. Chem. Reference Data* **1**, 1047–1100 (1972).
56. I. M. Abdulagatov, N. D. Azizov, Densities and apparent molar volumes of concentrated aqueous LiCl solutions at high temperatures and high pressures. *Chem. Geol.* **230**, 22–41 (2006).
57. M. A. Gebbie *et al.*, Ionic liquids behave as dilute electrolyte solutions. *Proc. Natl. Acad. Sci. U.S.A.* **110**, 9674–9679 (2013).
58. M. A. Gebbie, H. A. Dobbs, M. Valtiner, J. N. Israelachvili, Long-range electrostatic screening in ionic liquids. *Proc. Natl. Acad. Sci. U.S.A.* **112**, 7432–7437 (2015).
59. D. Xiong, H. Wang, Z. Li, J. Wang, Recovery of ionic liquids with aqueous two-phase systems induced by carbon dioxide. *ChemSusChem* **5**, 2255–2261 (2012).
60. M. Scott, B. Blas Molinos, C. Westhues, G. Franciò, W. Leitner, Aqueous biphasic systems for the synthesis of formates by catalytic CO2 hydrogenation: Integrated reaction and catalyst separation for CO2-scrubbing solutions. *ChemSusChem* **10**, 1085–1093 (2017).
61. X. Tian *et al.*, Design strategies of safe electrolytes for preventing thermal runaway in lithium ion batteries. *Chem. Mater.* **32**, 9821–9848 (2020).
62. J. Guilbert *et al.*, Label-free super-resolution chemical imaging of biomedical specimens. Preprint at 2021 (2021.05.14.444185), https://doi.org/10.1101/2021.05.14.444185.
63. X. Shi, N. Coca-López, J. Janik, A. Hartschuh, Advances in tip-enhanced near-field raman microscopy using nanoantennas. *Chem. Rev.* **117**, 4945–4960 (2017).
64. I. A. Heisler, S. R. Meech, Low-frequency modes of aqueous alkali halide solutions: Glimpsing the hydrogen bonding vibration. *Science* **327**, 857–860 (2010).
65. J. Bowers, A. Zarbakhsh, J. R. P. Webster, L. R. Hutchings, R. W. Richards, Neutron reflectivity studies at liquid—liquid interfaces: Methodology and analysis. *Langmuir* **17**, 140–145 (2001).
66. A. I. Kolesnikov *et al.*, Inelastic and deep inelastic neutron spectroscopy of water molecules under ultra-confinement. *J. Phys. Conf. Ser.* **1055**, 012002 (2018).
67. S. Nihonyanagi *et al.*, Unified molecular view of the air/water interface based on experimental and theoretical $\chi(2)$ spectra of an isotopically diluted water surface. *J. Am. Chem. Soc.* **133**, 16875–16880 (2011).
68. C.-C. Yu, T. Seki, Y. Wang, M. Bonn, Y. Nagata, Polarization-dependent sum-frequency generation spectroscopy for \AA{}ngstrom-scale depth profiling of molecules at interfaces. *Phys. Rev. Lett.* **128**, 226001 (2022).
69. Q. Cheng *et al.*, Operando and three-dimensional visualization of anion depletion and lithium growth by stimulated Raman scattering microscopy. *Nat. Commun.* **9**, 2942 (2018).
70. X. Peng *et al.*, Identification of a quasi-liquid phase at solid–liquid interface. *Nat. Commun.* **13**, 3601 (2022).
71. D. Degoulange *et al.*, Data associated to the manuscript "Direct Imaging of Micrometer Thick Interfaces in Salt-Salt Aqueous Biphasic Systems." *Zenodo*. https://doi.org/10.5281/zenodo.7782757. Accessed 6 April 2023.